

Modeling neural contrast sensitivity functions in human visual cortex

Carlien Roelofzen^{1,2,3*}, Marcus Daghlian^{1,2,3,4*}, Jelle A. van Dijk^{1,2}, Maartje C. de Jong^{1,2,5}, Serge O. Dumoulin^{1,2,3,6}

¹ Spinoza Centre for Neuroimaging, Amsterdam, Netherlands

² Computational Cognitive Neuroscience and Neuroimaging, Netherlands Institute for Neuroscience, Royal Netherlands Academy of Arts and Sciences, Amsterdam, Netherlands

³ Experimental and Applied Psychology, Vrije Universiteit Amsterdam, Amsterdam, Netherlands

⁴ Laboratory for Experimental Ophthalmology, University Medical Center Groningen, Groningen, Netherlands

⁵ Experimental and Applied Psychology, University of Amsterdam, Amsterdam, Netherlands

⁶ Experimental Psychology, Helmholtz Institute, Utrecht University, Utrecht, Netherlands

* shared first-author

Keywords

contrast sensitivity function, contrast response function, spatial frequency, visual cortex, fMRI

Abstract

The contrast sensitivity function (CSF) characterizes visual function, and is widely used in research on visual perception and ophthalmological disorders. The CSF describes the lowest contrast level that participants can perceive as a function of spatial frequency. Here, we present a new method to estimate the neural equivalent of the CSF that describes how a population of neurons responds to contrast as a function of spatial frequency. Using functional magnetic resonance imaging (fMRI) at 7 Tesla, we measured neural responses while participants viewed gratings that varied systematically in contrast and spatial frequency. We modeled the neural CSF (nCSF) using an asymmetric parabolic function, and we model the transition from no response to full response using a contrast response function (CRF). We estimated the nCSF parameters for every cortical location by minimizing the residual variance between the model predictions and the fMRI data. We validate the method using simulations and parameter recovery. We show that our nCSF model explains a significant amount of the variance in the fMRI time series. Moreover, the properties of the nCSF vary according to known systematic differences across the visual cortex. Specifically, the peak spatial frequency that a cortical location responds to decreases with

eccentricity and across the visual hierarchy. Furthermore, we observe that the slope of the CRF decreases with eccentricity, particularly in V1. This new method will provide valuable insights into the properties of the visual cortex and how they are altered in both healthy and clinical conditions.

1. Introduction

The detection of contrast and spatial frequency are fundamental aspects of vision. These features are important for object recognition and essential in everyday life. Where contrast is important in distinguishing an object from its background, spatial frequency reflects object size (Chung & Legge, 2016). The ability to detect a certain contrast is given by contrast sensitivity (100/contrast threshold) and depends on spatial frequency (Campbell & Robson, 1968; Lesmes et al., 2010; Sowden et al., 2002). The relation between contrast sensitivity and spatial frequency is described by the contrast sensitivity function (CSF). Behaviorally, the CSF defines the lowest contrast one can perceive as a function of spatial frequency (Campbell & Robson, 1968), thereby defining the threshold between the visible and invisible (Pelli & Bex, 2013).

The CSF is used to assess visual function. For example, the CSF is affected in many ophthalmological conditions, including amblyopia (Howell et al., 1983; Koskela & Hyvarinen, 1986; Sjöstrand, 1981; Wang et al., 2017), macular degeneration (Kleiner et al., 1988), optic neuritis (Zimmern et al., 1979), glaucoma (Ichhpujani et al., 2020), retinitis pigmentosa (Hyvärinen, 1983), cataract (Vasavada et al., 2014) and corneal edema (Hess & Garner, 1977). Additionally, the CSF can be altered in neurological conditions such as multiple sclerosis (Regan et al., 1981), cerebral lesions (Milling et al., 2014), Parkinson's disease (Ridder et al., 2017) and schizophrenia (Cimber et al., 2006).

In general, the CSF correlates with visual acuity (Hou et al., 2010; Stalin & Dalton, 2020). However, the CSF measures the detection of a stimulus using a wide range of contrasts and spatial frequencies, and has therefore been proposed as a more suitable tool to assess visual performance compared to standard visual acuity tests (Huang et al., 2007). For example, the CSF measures visual deficits missed by standard visual acuity tests. Thus, the CSF provides deeper insights regarding functional vision and improves detection of visual pathology (Huang et al., 2007; Lesmes et al., 2010).

The CSF characterizes visual perception and is altered by changes in the eye as well as changes in neural processing. In healthy participants, the CSF can be altered by cognitive manipulations such as attention, e.g. **contrast sensitivity is increased for attended stimuli and decreased for unattended stimuli (Pestilli et al., 2007)**. Furthermore, the CSF changes across development, during infancy as well as late childhood (Dekker et al., 2020). In addition, several

visual disorders are at least in part caused by neural deficits, for example amblyopia (Barrett et al., 2004) and glaucoma (Murphy et al., 2016). This highlights the relevance of studying neural processes underlying the CSF, in addition to the ocular components. Thus, a neural measure of the CSF would expand our understanding of how cortical processing is altered with cognition and different visual disorders.

Here, we translate the CSF from psychophysics, by introducing a new method that estimates the neural CSF (nCSF) in the human visual cortex using fMRI. This approach builds on previous studies showing that individual neurons in the visual cortex are sensitive to contrast and spatial frequency (Albrecht & Hamilton, 1982; Levitt et al., 1994; Sclar et al., 1990). This sensitivity is also present at the population level with fMRI studies showing systematic changes in contrast (Boynton et al., 1999; Marquardt et al., 2018), spatial frequency (Aghajari et al., 2020; Broderick et al., 2022; Henriksson et al., 2008; Singh et al., 2000; Sirovich & Uglesich, 2004) and their combination (Goulet & Farivar, 2024). Here we combine population measures of the CSF (akin to the population receptive field (pRF) method; Dumoulin & Wandell, 2008) and we model the transition from no response to full response, by varying the slope of the contrast response function (CRF, Boynton et al., 1999).

We show that our nCSF model explains a significant amount of the variance in the fMRI time series. Moreover, the properties of the nCSF vary systematically with eccentricity and across the visual hierarchy. Furthermore, the slope of the CRF decreases with eccentricity, particularly in V1. Overall, we describe a quantitative validated framework to model nCSF properties.

2. Methods

2.1 Participants

We present data from five participants (two males, age range 26-45 years). All participants had normal or corrected-to-normal visual acuity, as confirmed by testing visual acuity using a tumbling E eye chart. The participants gave written informed consent prior to the start of the experiment. The study was approved by the Ethical Committee of Vrije Universiteit Amsterdam in accordance with the World Medical Association's Declaration of Helsinki.

2.2 Stimulus presentation

The stimuli were generated using PsychToolbox (Brainard, 1997; Pelli, 1997) in MATLAB (version R2018b, Mathworks). Participants viewed the stimuli on a gamma corrected 32-inch BOLD screen display (Cambridge Research, 1920x1080 pixels), through an angled mirror

attached to the head coil (distance 220 cm). 10-bit mode was enabled on the BOLD screen display to facilitate presentation of stimuli with contrasts below 0.78% Michelson contrast. Participants were instructed to fixate on a dot in the center of the screen, and to press a button when the dot changed color.

The stimulus consisted of different static sinewave gratings with a circular aperture of 10.2 degree diameter of visual angle and raised cosine edge, presented on a mean luminance background. The gratings varied systematically in contrast and spatial frequency, see Figure 1. Each stimulus block lasted 18 s and consisted of gratings with the same spatial frequency but systematically changing (either decreasing or increasing) in contrast (Figure 1A). Three different gratings were shown every 1.5 s with the same contrast but a different orientation (Figure 1B). Twelve different contrasts were used in each stimulus block, ranging from 0.25-80% Michelson contrast. An increasing and decreasing contrast block was included for each spatial frequency (0.5, 1, 3, 6, 12, 18 c/deg), and the order in which these blocks were presented was fixed, see Figure 1A. Before every two stimulus blocks there was a mean luminance block lasting for 15 s, and there was an extra 15 s mean luminance block in the end. The orientation of the gratings was randomized, and two subsequent gratings had at least a 45 degree difference in orientation. Each grating presentation lasted for 300 ms and was followed by a 200 ms presentation of mean luminance (see Figure 1B). The total stimulus protocol lasted 321 s per run. The contrast range presented was dependent on the spatial frequency shown in the stimulus block, ensuring an optimal sampling of the CSF (see Figure 1C, and Supplementary Materials, Table S1).

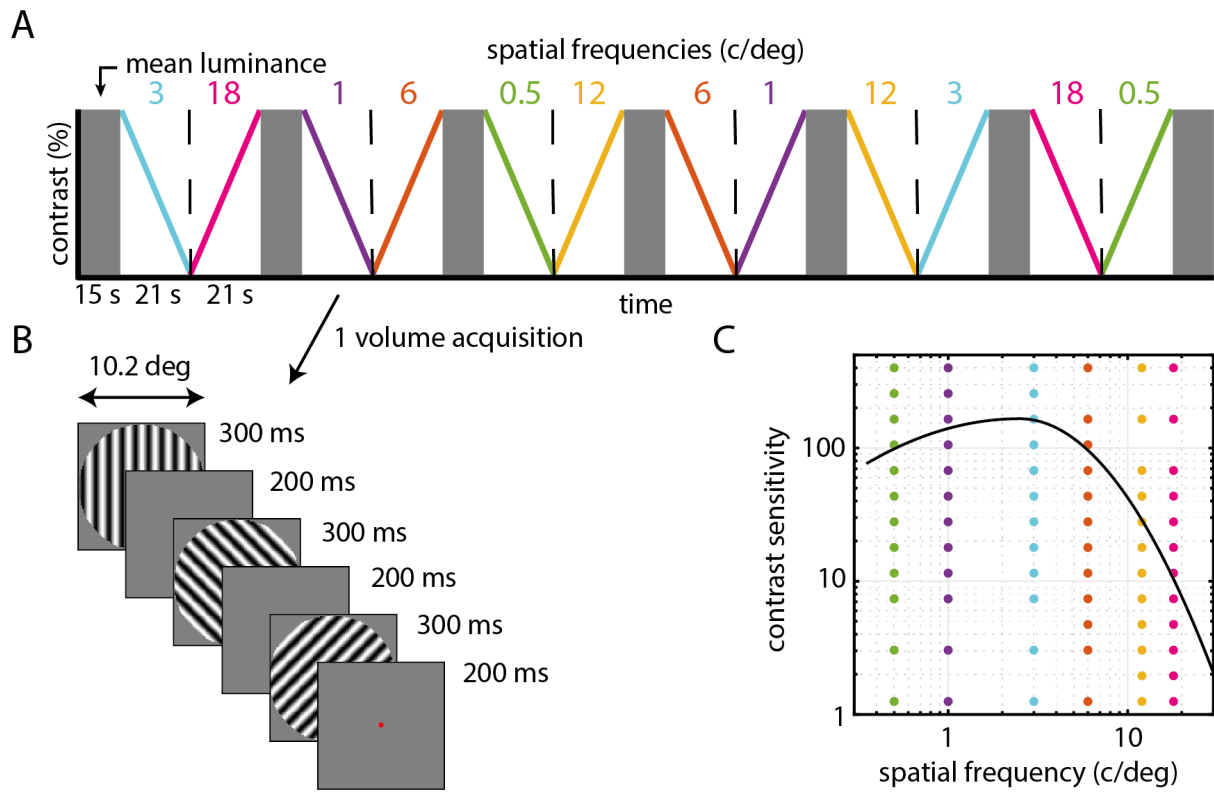


Figure 1. Schematic representation of the stimulus design.. A) We presented full-field static sinewave gratings with six different spatial frequencies (0.5, 1, 3, 6, 12, 18 c/deg). Gratings with the same spatial frequency are presented in both in descending contrasts and ascending contrasts in a fixed semi-random order. B) During every MRI volume acquisition (1.5 s), three gratings with the same contrast but a different orientation were shown. Each grating presentation lasted for 300 ms followed by mean luminance lasting 200 ms. The participants fixated the red dot. C) A typical CSF curve with dots showing the stimulus sampling grid across spatial frequency and contrast.

2.3 Data acquisition

Anatomical and functional magnetic resonance imaging (fMRI) data were acquired on a 7 Tesla Philips Achieva scanner (Philips, Best, Netherlands) with an 8-channel MultiX head coil. Anatomical images were collected using a 3D MP2RAGE sequence (TR = 6.2 ms, TE = 3.0 ms, flip angle = 5.0 degrees, FOV = 220 x 220 x 164 mm, voxel size = 0.7 mm isotropic) (Marques et al., 2010).

fMRI data was acquired using a T2*-weighted 2D echo-planar imaging (EPI) sequence (TR = 1.5 s, TE = 22.5 ms, flip angle = 65 degrees, FOV = 216 x 216 x 97 mm, 57 slices, voxel size = 1.7 mm isotropic) oriented across the visual cortex. For each participant 10-12 functional scans were acquired, with an approximate duration of 5 minutes per functional run. Each functional run was followed by a TOPUP scan in order to correct for local image distortions. Additionally, pRF data was collected for one participant (8 functional runs) with the same

sequence for visual field mapping (see *Region of interest definition*), For the remaining four participants, pRF mapping data was already available.

2.4 Data pre-processing

For the anatomical data, the MP2RAGE sequence was used to obtain a T1-weighted anatomical image resulting in a set of different gradient echo images, i.e. the first inversion (T1-weighted image) and a second inversion (proton density scan). The first and second inversion were combined to generate a single anatomical image, corrected for proton density. The anatomical image was skull-stripped using the *3dSkullstrip* function in AFNI (Cox, 1996). Segmentation of gray and white matter was performed using CBS Tools in MIPAV (Bazin et al., 2007). The cortical surfaces for each participant were reconstructed using the FreeSurfer 7.2 *recon-all* function (Dale, 1999). To improve the FreeSurfer reconstructions particularly around the sinus, segmentations from CBS Tools were added to Freesurfer's "*brainmask.mgz*" file, and *recon-all* was run again.

For the functional data, all functional images were pre-processed using AFNI. The warp field of all functional images was estimated based on the EPI and TOPUP of each run to correct for susceptibility distortions. The motion parameters were calculated to apply motion correction to all functional images. Then, all warped and motion corrected volumes were combined to generate an average EPI image. This EPI image was registered to the anatomical image. The volume of the mean EPI image was masked using the AFNI function *3dAutomask* to reduce volume size, and was zero-padded using *3dZeroPad*. The center of mass of the anatomical volume was aligned to the mean EPI image using *@Align_centers* to improve co-registration. Then, the mean EPI image was manually shifted and rotated using the *Nudge dataset* AFNI plugin, after which the automated registration function *3drotate* optimized the co-registration using affine transformation. The co-registration was then applied to all EPI images of all individual functional runs using the function *3dNwarpApply* with nearest-neighbor interpolation. The co-registered functional volumes were then projected to the participant's cortical surface using the *mri_vol2surf* function in FreeSurfer (Dale, 1999). Veins were identified by displaying the mean EPI signal on the cortical surface, and masking those vertices with relatively low signal intensity. The BOLD time series were then detrended by demeaning, applying the discrete cosine transform (DCT), removing the first three DCT coefficients to eliminate low-frequency trends. The detrended data were further processed by averaging over functional runs and converting to BOLD percent signal change.

2.5 Model-based analysis

The nCSF model combines the contrast sensitivity function (CSF) with the contrast response function (CRF) and aims to fit the CSF in each cortical location (voxel), thereby obtaining the nCSF (Figure 2). The CSF is described by Chung & Legge (2016) and is characterized as an asymmetric parabolic function with the following equation:

$$f(SF) = \begin{cases} CS_p - (SF - SF_p)^2 \times (width_L)^2 & \text{if } SF < SF_p, \\ CS_p - (SF - SF_p)^2 \times (width_R)^2 & \text{if } SF \geq SF_p \end{cases} \quad (\text{Equation 1})$$

Where $f(SF)$ is the contrast sensitivity at spatial frequency (SF), CS_p is the peak contrast sensitivity, and SF_p is the spatial frequency at which CS_p occurs (peak spatial frequency), and $width_L$ and $width_R$ are the curvatures of the left and right branches of the asymmetric parabolic function, respectively (Chung & Legge, 2016). The $width_L$ is set at 0.68 (Chung & Legge, 2016) and $width_R$ is varied as a model parameter, since we expect the most variance on the right branch at higher spatial frequencies ($SF > SF_p$). The maximum spatial frequency (SF_{max}) can be determined where $f(SF)$ equals 1 (or 10^0 in \log_{10} space). We report the normalized area under the log contrast sensitivity function (AUC , %) as a summary metric of the full CSF for spatial frequencies between 0.5-18 c/deg (stimulus space). AUC is calculated by approximating the integral of the logarithmic CSF, and normalizing it with reference to the area under a “standard” logarithmic CSF calculated from healthy controls (from Chung & Legge, 2016: $CS_p = 166$, $SF_p = 2.5$ (c/deg), $width_L = 0.68$, $width_R = 1.28$, shown in Figure 1C).

The parameters SF_p and CS_p are transformed to \log_{10} space before fitting the CSF (Equation 1, Chung & Legge, 2016). Here we used an adapted version of Equation 1 where all parameters are defined in linear space before fitting the CSF:

$$f(SF) = \begin{cases} 10^{\log_{10}(CS_p) - (\log_{10}(SF) - \log_{10}(SF_p)) \times (width_L)^2}, & \text{if } SF < SF_p \\ 10^{\log_{10}(CS_p) - (\log_{10}(SF) - \log_{10}(SF_p)) \times (width_R)^2}, & \text{if } SF \geq SF_p \end{cases}$$

For transforming the binary response of the CSF to a gradual response, we added the CRF to the nCSF model (Figure 2). We fitted CRFs using the following equation (modified from Boynton et al., (1999)):

$$R(C) = \frac{C^q}{C^q + Q^q} \quad (\text{Equation 3})$$

Where R is the fMRI response and C is the amount of RMS-contrast. The variables for Q and q define the shape of the CRF. Q represents the contrast where the fMRI response is at 50%, and was depended on the CSF. We fitted the variable q or $slope_{CRF}$.

The nCSF parameters were estimated from the fMRI data using a model-based fitting approach (Figure 2), similar to the population receptive field (pRF) method (Dumoulin & Wandell, 2008). First, the fMRI blood oxygen level dependent (BOLD) response is predicted through multiplying the nCSF model with the stimulus sequence and convolving the time course with the hemodynamic response function (HRF). Here the HRF was modeled using the two gamma basis functions (Glover, 1999). The coefficients corresponding to the canonical HRF, its derivative, and dispersion were fixed at values of 1, 1, and 0, respectively (Pedregosa et al., 2015). The same HRF was used in both fitting the nCSF and pRF model. We varied the model parameters (CS_p , SF_p , $width_R$ and $slope_{CRF}$) in a coarse-to-fine manner. All model parameters are varied until the residual sum-of-squares (RSS) is minimized between the predicted and measured fMRI data, thereby maximizing the variance explained (r^2) of the model. The nCSF model was fitted to all cortical locations (voxels) independently. We selected cortical locations with $r^2 > 30\%$ for further analyses.

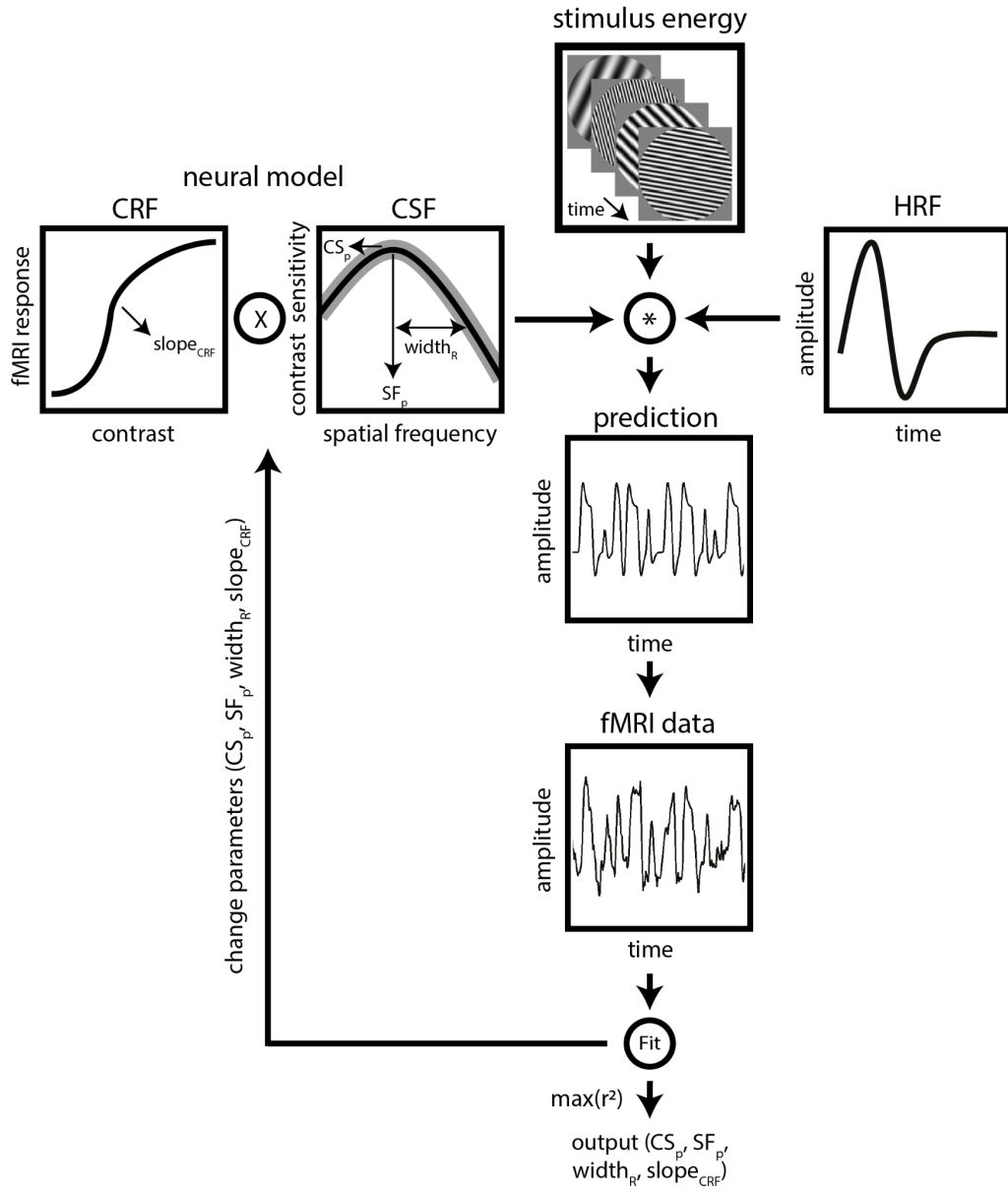


Figure 2. Schematic overview of the nCSF model-based analysis. The nCSF model combines the CSF (Chung & Legge, 2016) with the CRF (Boynton et al., 1999). We predict the fMRI response by a multiplication of the nCSF model with the stimulus sequence, and convolve this model time course with the HRF. We vary the slope of the CRF ($slope_{CRF}$) and the CSF parameters (CS_p , SF_p and $width_R$). The optimal model parameters are estimated by maximizing the variance explained (r^2) between the predicted and measured fMRI time series, similar to the pRF method (Dumoulin & Wandell, 2008).

2.6 Region of interest definition

For the region of interest (ROI) definition pRF mapping was used (Dumoulin & Wandell, 2008). This data was already available for four participants, and we collected pRF data for one participant (see *Data acquisition*). We included visual field maps V1, V2, V3, hV4 and visual field map clusters TO, LO, and V3AB as ROIs (Wandell et al., 2007).

2.7 Model validation

We validated the method using simulations (Dumoulin & Wandell, 2008; Lerma-Usabiaga et al., 2020), where the ground truth is known, and estimated the accuracy through model parameter recovery. To validate the nCSF model, we simulated four of nCSF models: two nCSF models with different CSF parameters, but identical CRF parameters (in green: $SF_p = 1$ c/deg, $CS_p = 150$, $width_R = 1.3$, $slope_{CRF} = 1.5$, in red: $SF_p = 2$ c/deg, $CS_p = 100$, $width_R = 1$, $slope_{CRF} = 1.5$); and two nCSF models with the same set of CSF parameters were chosen but with a different CRF (in cyan: $SF_p = 2$ c/deg, $CS_p = 100$, $width_R = 1$, $slope_{CRF} = 1.5$, in blue: $SF_p = 2$ c/deg, $CS_p = 100$, $width_R = 1$, $slope_{CRF} = 3$), see Figure 3.

For each simulated dataset, the predicted response was calculated using the stimulus sequence (as described in *Stimulus presentation*) and combination of model parameters, convolved with the standard HRF. We normalized these synthetic voxel time series and added three different noise levels. Noise was generated by sampling from a normal distribution ($M = 0$, $SD = 1$) multiplied by a scaling factor 0.4, 0.7, or 1.1. For each noise level and combination of model parameters, 100 time series were generated. Next, we fitted the nCSF model using the same HRF used for the main data analysis (see *Model-based analysis*). The model parameters were extracted from the simulated datasets, and the variance explained for each of the three noise levels was computed, resulting in the low, medium and high variance explained categories. The two different nCSF curves and two different CRFs for the three variance explained categories are shown in Figure 3. Additionally, we simulated the effect of the HRF on the model parameters (see Supplementary Materials, *HRF simulation*).

3. Results

3.1 Validation of nCSF model-based analysis

Validation is essential for method development (Aqil et al., 2021; Dumoulin et al., 2003; Dumoulin & Wandell, 2008). Modern data-analyses techniques are complex and it is impossible to check the software by eye: ground truth datasets are needed (Lerma-Usabiaga et al., 2020). Here we validated the nCSF model using simulations.

We compared two nCSF models with different parameters and signal-to-noise ratios, but identical CRF parameters (see *Methods*). In all signal-to-noise categories, resulting in different variance explained levels (see Figure 3A-C), the median estimated nCSF curves (dashed lines in red and green) closely match the true curve (solid lines in red and green). Increased noise levels, resulted in lower variance explained and more deviations of the estimated nCSF curves from the true curve (compare Figure 3A-C).

We also compared two nCSF models with the same set of CSF parameters but with a different CRF, i.e. $slope_{CRF}$ (either 1.5 or 3). The $slope_{CRF}$ of both the median CRFs (blue and cyan in Figure 3D-F) is overestimated in the lowest variance explained level (see Figure 3F), when comparing the median value of the 100 repetitions (dashed lines) versus the true value (solid lines). In the medium and high variance explained categories (see Figure 3D-E) the median CRFs (dashed lines) closely follow the true CRFs (solid lines), but with a larger variability of CRFs above the median and true CRFs. This indicates that the CRF is more likely to be overestimated (i.e. a higher $slope_{CRF}$) when more noise is added.

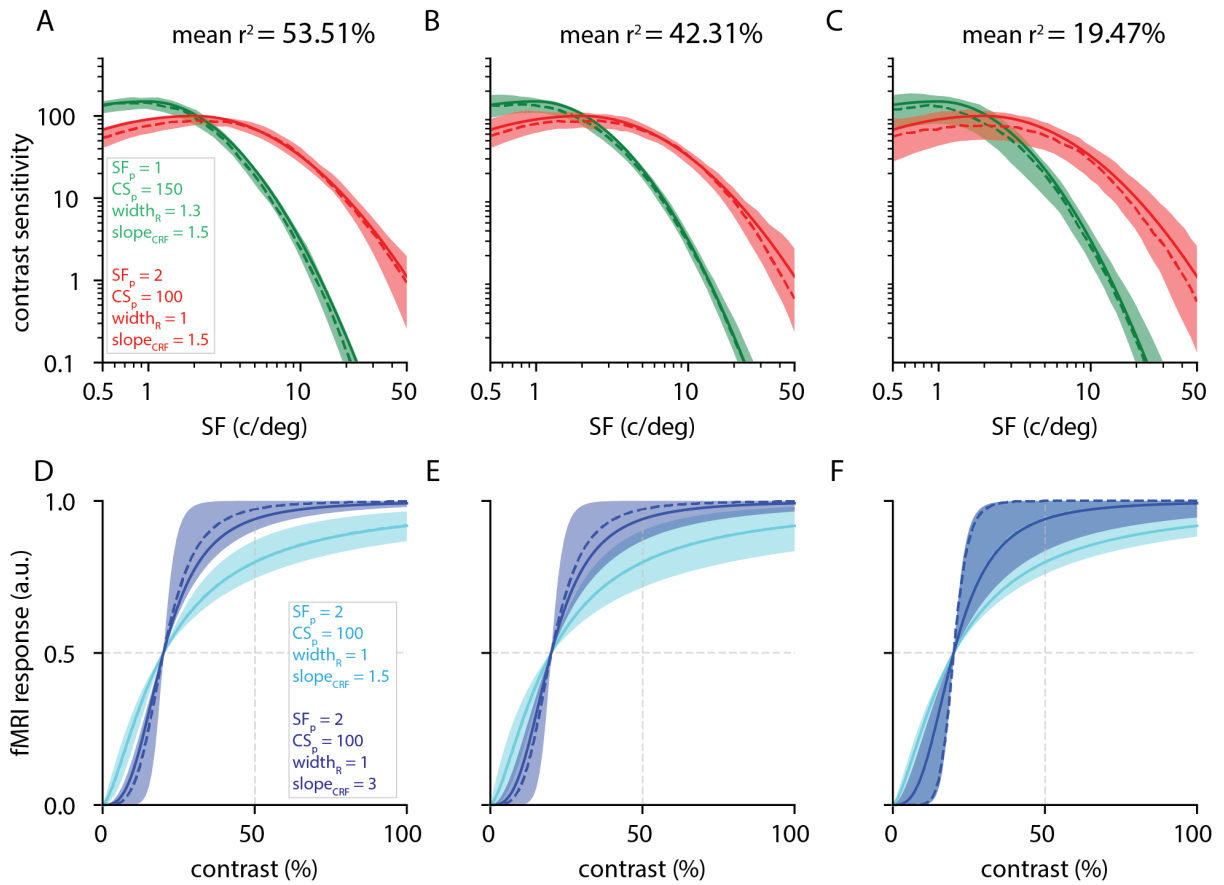


Figure 3. nCSF model validation. We tested different combinations of nCSF model parameters: two sets of nCSF parameters with a different CSF but same CRF (panels A-C, red and green), two sets of nCSF parameters with the same CSF but different CRF (panels D-F, cyan and blue). For each combination of parameters, the results are shown for synthetic data (100 permutations) and three variance explained categories (mean $r^2 = 53.51\%$, mean $r^2 = 42.31\%$, mean $r^2 = 19.47\%$, left to right, respectively). The solid lines represent the nCSF curves based on the chosen parameters, the dashed lines represent the median nCSF curves, the shaded areas represent the 95% confidence interval. Note for CRF figures (panels D-F) the response values (a.u.) are calculated using *Equation 3* (see *Methods*) with $Q = 20\%$. All subsequent CRF figures follow the same format.

In the simulations, the median values of the fitted parameters closely match the ground truth values. The spread of the fitted parameters increases from high to low variance explained levels (see Figure 4). There are no apparent biases in fitted parameters, except for $slope_{CRF}$, which tends to be slightly overestimated at higher noise levels (see Figure 4D,H).

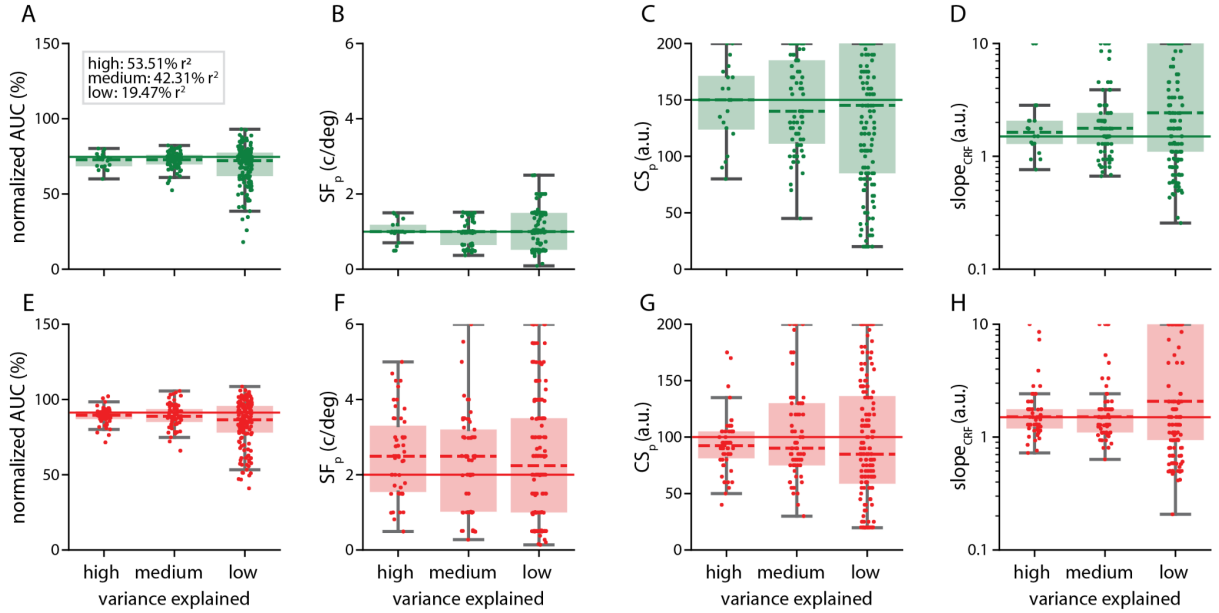


Figure 4. nCSF model parameter recovery. The solid lines indicate the true nCSF model parameters, whereas the dashed lines and distributions represent the median values of 100 permutations. For each model parameter the effect is shown for the high, medium and low variance explained category (left to right, respectively). A) and E) Normalized AUC (%), output variable. B) and F) SF_p (c/deg). C) and G) CS_p (a.u.). D) and H) $slope_{CRF}$ (a.u.). Overall, the nCSF fit recovers the parameters, but the variability increases with increasing noise (lower variance explained). Some parameters, in particular normalized AUC (%), output variable) and SF_p (c/deg), are more stable than others (in particular CS_p).

3.2 nCSF model captures responses across the visual hierarchy

We fitted the nCSF model to the fMRI time series in each cortical location. Cortical locations in TO and V1 respond differently to the same stimulus (see Figure 5). The variation between the cortical locations can be explained by the nCSF model, resulting in different CSFs and CRFs for a cortical location in TO and V1 (see Figure 5B-C). The $slope_{CRF}$ value for the cortical location in V1 is higher compared to the cortical location in TO, indicating a more binary response to contrast (see Figure 5B). The modeled CSFs are different between the cortical locations, the cortical location in V1 has a higher SF_p and lower CS_p compared to the cortical location in TO. The variance explained for the cortical locations in TO and V1 was 67.47% and 63.35% respectively, indicating that the nCSF model captures the variance in the fMRI time series similarly.

Additionally, the predicted fMRI time series match the recorded fMRI time series well (see Figure 5D-E).

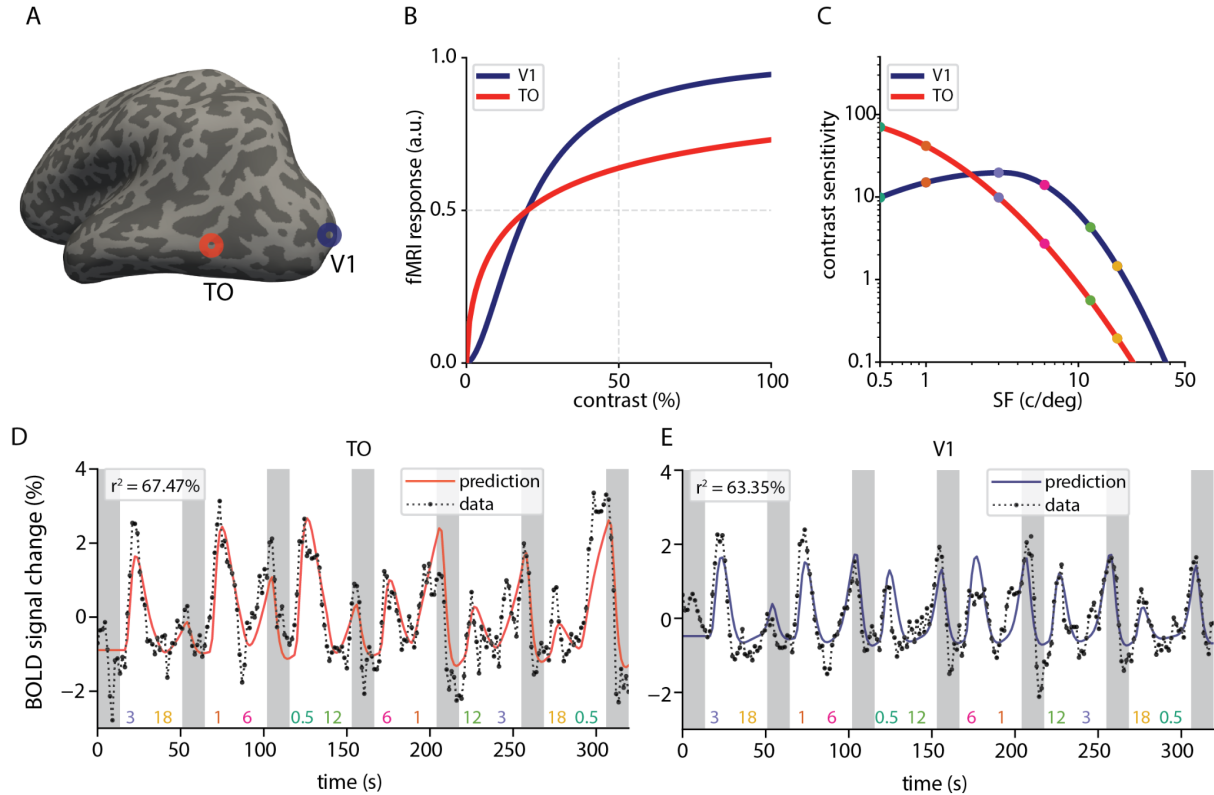


Figure 5. Example fMRI time series and nCSF model fits. A) Inflated cortical surface (left hemisphere) showing the location of the example cortical locations in V1 (blue circle) and TO (red circle). B) CRFs for example cortical locations in V1 (blue) and TO (red), demonstrating how the fMRI response amplitude changes with contrast. C) nCSF for example cortical locations in V1 (blue) and TO (red). Each dot represents one of the spatial frequencies used in the stimulus sequence. D) fMRI time series of a vertice in TO (black dotted line) and nCSF model fit (red line). E) fMRI time series for a vertice and V1 (black dotted line) and nCSF model fit (blue line).

3.3 nCSF properties vary across the cortex

The ROIs and eccentricity maps derived from pRF mapping for one participant are shown on the inflated cortical surface in the region near the occipital pole, see Figure 6A,B. The eccentricity maps range from 0-5 degrees of visual angle, indicating the visual field representation. nCSF parameter and outcome estimates are projected on the inflated cortical surface, see Figure 6C-F.

The variance explained of the nCSF model is high across eccentricities and ROIs, see Figure 6C. The normalized *AUC* is high around the foveal region and generally decreases with eccentricity (Figure 6D). SF_p is also higher near the foveal region compared to the parafoveal region and decreases as a function of eccentricity (see Figure 6E, 7D,I), consistent with previous studies (Aghajari et al., 2020; Broderick et al., 2022; Henriksson et al., 2008). The $slope_{CRF}$ is also

higher near the foveal region compared to the parafoveal region (see Figure 6F), indicating a more binary response to contrast in cortical locations near the foveal regions. We observe that these systematic changes are similar between ROIs and participants (see Supplementary Materials, Figure S6).

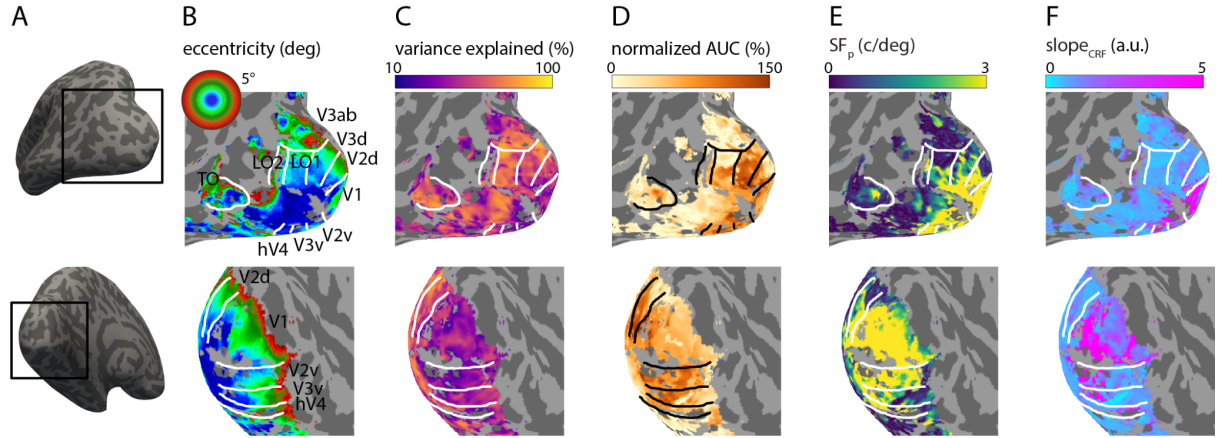


Figure 6. nCSF model parameters displayed on the cortical surface. Parameters are shown for participant 1 (see appendix for figures showing all participants' surfaces). We included cortical locations with variance explained >10% for visualization. A) Inflated cortical surface (left hemisphere) and ROIs with the lateral (top row) and medial (bottom row) views. Black boxes indicate the zoomed views for panels B-F. B) Eccentricity (deg, from pRF mapping data) for comparison with nCSF parameters. Borders of ROIs (white lines) are displayed (V1, V2, V3, V3ab, hV4, LO, TO). C) Variance explained (r^2 %) of nCSF fits is high across ROIs and eccentricities. Panels D-F display nCSF model parameters: D) Normalized *AUC* (%), output variable. E) SF_p (c/deg). F) $slope_{CRF}$ (a.u.).

3.4 nCSF properties vary with eccentricity and the cortical hierarchy

The median nCSFs (with 25th and 75th percentiles) for V1 and different eccentricity bands for three participants are shown in Figure 7A-C (for the other participants see Supplementary Materials, Figure S3). CS_p is different across participants in V1. However, in all participants there is a shift in SF_p between different eccentricity bands. SF_p in V1 is highest for the eccentricity band containing eccentricities between 0-1 degrees, lower for the eccentricity band containing eccentricities between 2-3 degrees, and lowest for the eccentricity band containing eccentricities between 4-5 degrees.

To determine how nCSF parameters vary with eccentricity (see figures 7D, 7E and 8C), we used linear regression analysis to fit the slope of eccentricity versus SF_p , normalized *AUC*, and $slope_{CRF}$. This analysis was performed separately per participant, using only cortical locations (vertices) in V1 where the nCSF model fit had a variance explained >30%. To correct for volume-to-surface upsampling, we determined the degrees of freedom used in calculating the t-statistics by taking the number of cortical locations (vertices) divided by the upsampling

factor. SF_p decreases as a function of eccentricity in V1 for all participants, $p < 0.001$ (see Figure 7D and Supplementary Materials, Table S2). The normalized AUC also decreases with eccentricity in V1 for all participants, $p < 0.001$ (see Figure 7E and Supplementary Materials, Table S2).

Additionally, we computed the median nCSFs for V1, V2 and V3 for one participant, see Figure 7F-H). SF_p is higher for eccentricities between 0-1 degrees, compared to the higher eccentricity bands (between 2-3 degrees and 4-5 degrees). This effect is similar between V1, V2 and V3. However, in V2 and V3 there is more variation between nCSFs compared to V1.

We observed differences in SF_p versus eccentricity across the visual hierarchy in participant 1, see Figure 7I. We found that SF_p decreases as a function of eccentricity. This trend is more pronounced in the early visual cortex (V1, V2, and V3) compared to higher visual areas (hV4 and LO). In V3ab and TO, SF_p remained mostly constant. We observed a similar pattern for normalized AUC , see Figure 7J. The normalized AUC decreases as a function of eccentricity, this decrease is more pronounced in the early visual cortex (V1, V2, V3), compared to higher visual areas (hV4, LO, TO). In V3ab, normalized AUC remained mostly constant. We found a similar pattern for all participants, see Supplementary Materials, Figure S5. However, note that we only included cortical locations (voxels) with eccentricities up to 5 degrees of visual angle (the stimulus range), so these results might be slightly different when using a stimulus with a larger visual field representation.

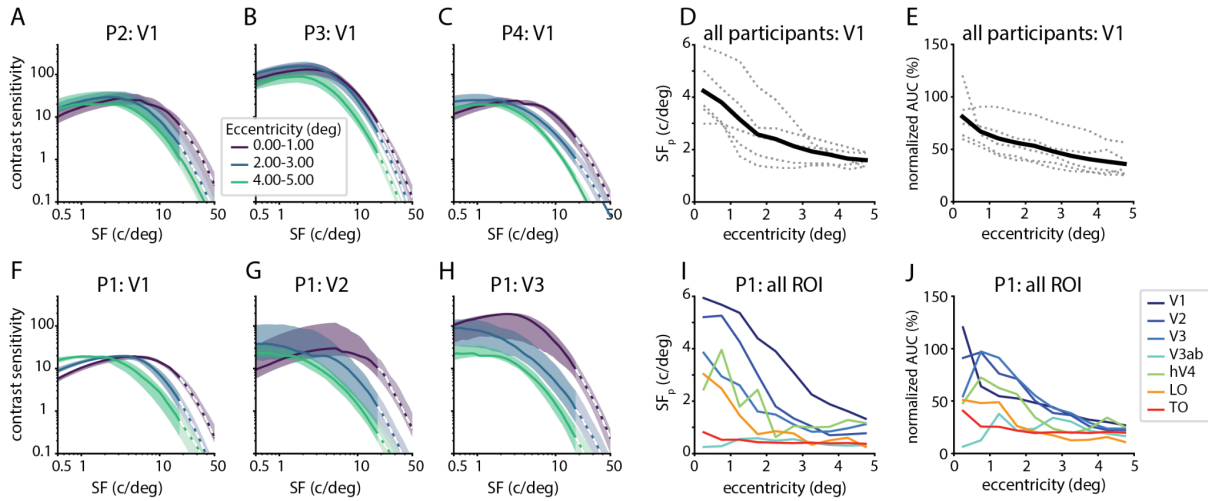


Figure 7. Variation in nCSF properties across eccentricity and the cortical hierarchy. A), B) and C) nCSF fits for cortical locations inside V1 for participants 2, 3 and 4, respectively. nCSF fits are split by eccentricity band (from pRF mapping: 0-1 degrees, 2-3 degrees, 4-5 degrees eccentricity; represented by purple, blue and green lines, respectively). Solid lines represent the median nCSF for all cortical locations within a given ROI and eccentricity band (where $r^2 > 30\%$). Shaded regions represent the 25th and 75th percentile of the nCSFs. We extrapolated the nCSF beyond the range of spatial frequencies present in the stimuli (>18 c/deg), where this has been done the lines become dotted and the shading becomes lighter. D) and E) SF_p (c/deg) and normalized AUC (%) decrease with eccentricity (deg) respectively across all participants (mean = thick black line, individuals = dotted gray lines); lines are the mean value binned by eccentricity (bin width = 0.5 deg). F), G) and H) same format as panels A-C, but for a single participant (P1) across areas V1, V2, and V3 respectively. I) and J) SF_p (c/deg) and normalized AUC (%) vary with eccentricity (deg), across ROIs for P1. Both SF_p (c/deg) and normalized AUC (%) decrease with eccentricity (deg), and up the cortical hierarchy.

3.5 CRF properties vary with eccentricity in V1 and between V1 and extrastriate cortex

We included the CRF in the nCSF model and varied the $slope_{CRF}$, see Methods and *Equation 3*. For the highest eccentricity band (4-5 degrees), $slope_{CRF}$ is lower compared to the lower eccentricities (0-1 degrees and 2-3 degrees) for two example participants (Figure 8A,B). The CRFs for other participants and ROIs beyond V1 are shown in Figure S4. Linear regression analysis showed a negative relationship between $slope_{CRF}$ and eccentricity in V1 for 3 out of 5 participants ($p < 0.01$, see Supplementary Materials, Table S2).

We observed differences in the CRFs between ROIs. $slope_{CRF}$ is higher for V1 (Figure 8D) compared to TO (Figure 8E), indicating a sharper response to contrast in V1. In general, $slope_{CRF}$ is higher for V1 compared to the other ROIs (V2, V3, V3ab, hV4, LO and TO) and the effect of eccentricity is more pronounced in V1, see Figure 8F. We found a similar pattern for the other participants (see Figure S5).

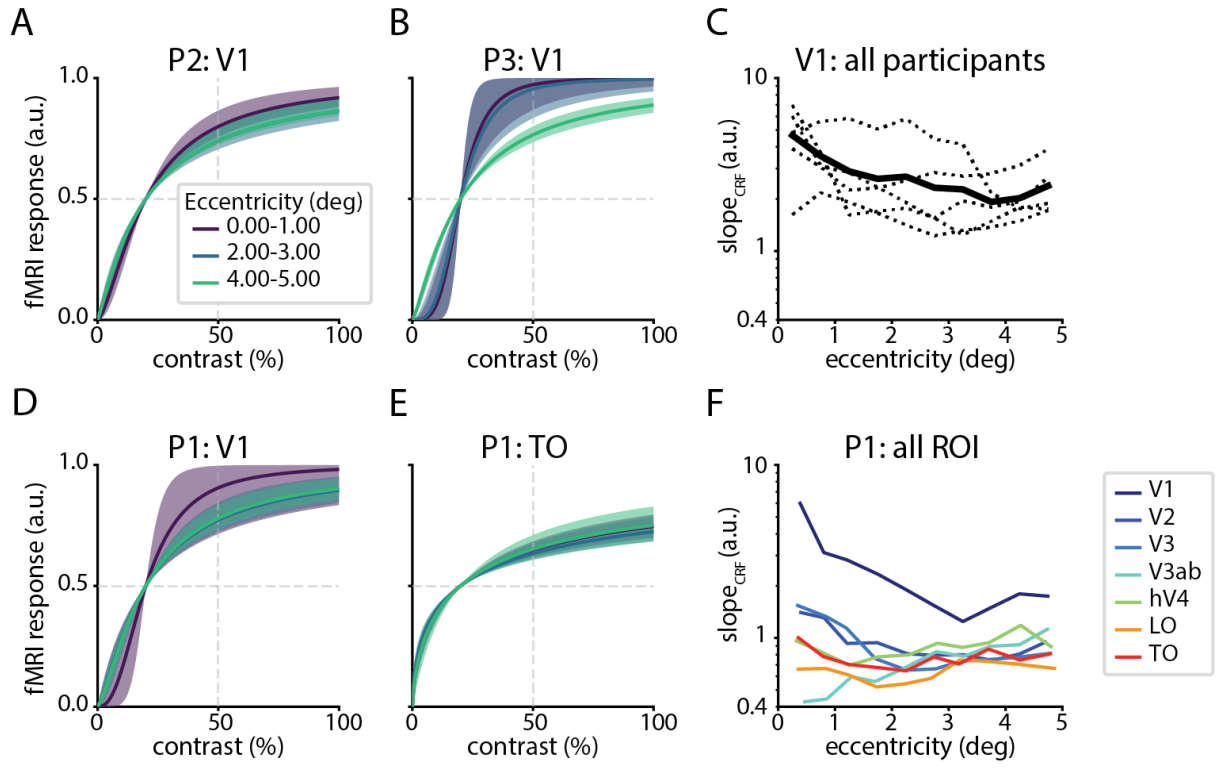


Figure 8. Variation in CRF properties across eccentricities and the cortical hierarchy. A) and B) CRF fits for V1 for participants 2 and 3. CRF fits are split by eccentricity bands (0-1 degrees, 2-3 degrees, 4-5 degrees; represented by purple, blue and green lines, respectively). Solid lines represent the median CRF (where $r^2 > 30\%$). Shaded regions represent the 25th and 75th percentile of the CRFs. C) In V1, $slope_{CRF}$ decreases with eccentricity in 3 out of 5 participants (mean = thick black line, individuals = dotted gray lines). D) and E) same format as panels A and B, but for a single participant (P1) across areas V1 and TO. F) $slope_{CRF}$ varies with eccentricity across ROIs for P1.

4. Discussion

We introduce the concept of the neural contrast sensitivity function (nCSF). The nCSF is both a concept and a method. As a concept, the nCSF describes the sensitivity of neural populations as a function of spatial frequency and contrast. As a method, we model the nCSF in the human visual cortex using fMRI using an approach similar to pRF modeling (Dumoulin & Wandell, 2008). The nCSF parameters were estimated from the fMRI data using a biologically-inspired, model-based approach similar to the pRF method. We model nCSF properties using a combination of the CSF (Chung & Legge, 2016) and CRF (Boynton et al., 1999).

We validated this nCSF method using simulations. The nCSF model captured the variance in the fMRI data and obtained robust model estimates. We found that the peak spatial frequency and area under the nCSF both decrease as a function of eccentricity. This effect was similar

across the visual cortex, but more pronounced in early visual cortex (V1, V2, V3) versus late visual cortex (e.g. LO and TO).

These results regarding nCSF peak spatial frequency are consistent with previous fMRI studies (Aghajari et al., 2020; Henriksson et al., 2008). Many factors may lead to changes in nCSF properties, for example using different stimuli or tasks. Different stimuli, e.g. different temporal characteristics, may elicit responses from different neural populations and therefore result in different nCSF. Likewise, attention influences the nCSF, and therefore different tasks may influence the nCSF (Cameron et al., 2002; Jigo & Carrasco, 2020). Additionally, nCSF estimates could also vary with polar angle. Contrast sensitivity is higher around the horizontal meridian compared to the vertical meridian (Himmelberg et al., 2020, 2022). Thus, the pRF model the stimuli and task are likely to influence the neural population driving the responses underlying the nCSF model.

We observed that CRF varies with eccentricity and the visual hierarchy. Specifically, the slope of the CRF decreases with eccentricity in V1. We also find that the CRF is different between V1 and the extrastriate cortex. The CRF is known to be different between V1 and extrastriate cortex from electrophysiology (Albrecht & Hamilton, 1982; Levitt et al., 1994; Sclar et al., 1990) and fMRI (Avidan et al., 2002; Boynton et al., 1999; Tootell et al., 1995; Vinke et al., 2022), but typically most shallow in V1. We find steeper slopes in V1 which seem at odds with previous results. We speculate that this may be a consequence of our model design. For example, as the sensitivity of the nCSF increases, i.e., reaches 50% of maximal contrast at lower contrasts, the CRF likely increases. In other words, the CRF function is bound at 0% contrast with 0% response and the contrast at which 50% is reached. The closer these two get together, the steeper the slope must get and there is less space for the slope of the contrast response curve to change. This result may change if the relationship between the nCSF and CRF are altered in the nCSF model.

We can extend the nCSF model. We used a basic model to estimate the nCSF, which has the advantage that parameters are interpretable and have a clear relation to psychophysics. However, the model could be extended, akin to the pRF model (Dumoulin & Wandell, 2008), which was extended, for example to include suppression (Zuiderbaan et al., 2012), compression (Kay et al., 2013) and divisive normalization (Aqil et al., 2021). Furthermore, for clinical conditions the pRF model has been extended to capture atypical pRF layouts (Dumoulin & Knapen, 2018; Hoffmann et al., 2012; Hoffmann & Dumoulin, 2015). Likewise, to capture pRF deviations from the models, model-free approaches evolved (Carvalho et al., 2020; Greene et al., 2014; Lee et al., 2013). However, in all cases, the basic pRF model laid the foundations. Using a basic model has the advantage that the model parameters are easily interpretable without

complex interactions between model parameters. Like the conventional single Gaussian pRF model, here we propose a basic model of the nCSF.

The nCSF method combined with fMRI measures responses from populations of neurons rather than single neurons. This is similar to the concept of the pRF that represents a statistical summary of all contributions of the single neuron receptive fields (Dumoulin & Wandell, 2008). Given estimates of neuronal packing density (Leuba & Garey, 1989; Rockel et al., 1980) each recording location contains about between 10 to 10^5 neurons (Leuba & Garey, 1989). The nCSF has been investigated using single cell recordings (Movshon et al., 1978). However, the properties of the nCSF represent a statistical summary of the properties of the neural population. The size of the neural population may vary depending on the resolution and measurement modality. Likewise, the stimulus properties may elicit responses from a selection of these neurons. Thus, the nCSF of neural populations is related to single neurons but not identical, as the size and heterogeneity of the neural population will influence the population properties.

The nCSF model is inspired by psychophysics, where the CSF is widely used in health and disease (Chung & Legge, 2016; Lesmes et al., 2010; Pelli & Bex, 2013). However, neural responses do not necessarily follow perception. Neural CSFs vary across the cortex and may - at varying levels of the processing hierarchy - differ from perceptual CSFs. Patients may have deficits in the neural CSF in a specific brain region which are not present in the perceptual CSF and vice versa. Therefore it is important to investigate both perceptual and neural measures in health and disease.

5. Conclusion

We introduce a novel method to measure the nCSF in the human visual cortex. We provide a quantitative, validated framework and show how nCSF properties vary across visual field maps and with eccentricity. This method can be applied to both healthy and clinical conditions, and provide novel insights into the cortical organization underlying perception.

Declaration of competing interest

The authors declare no competing interest.

Acknowledgements

This research was supported by Dutch Research Council Vici Grant 016.Vici.185.050 (to S.O.D.).

Author contributions

S.O.D. and C.R. conceived the study. C.R. collected the data. C.R., M.D., J.D. analyzed the data. C.R. wrote the paper. M.D., M.J. and S.O.D. edited the paper. S.O.D. and M.J. provided supervision.

Data and code availability statement

The code generated for this paper is available here:

https://github.com/spinoza-centre/prfpy_csenf

The data is considered personal data pursuant to the General Data Protection Regulation (GDPR) and can only be shared based on and subject to the policies of the Royal Netherlands Academy of Arts and Sciences (KNAW). The datasets are available from the corresponding author on request. Considering the requirements imposed by law and the sensitive nature of personal data, any requests will be addressed on a case-by-case basis, subject to a data usage agreement.

References

- Aghajari, S., Vinke, L. N., & Ling, S. (2020). Population spatial frequency tuning in human early visual cortex. *Journal of Neurophysiology*, 123(2), 773–785.
<https://doi.org/10.1152/jn.00291.2019>
- Albrecht, D. G., & Hamilton, D. B. (1982). Striate cortex of monkey and cat: Contrast response function. *Journal of Neurophysiology*, 48(1), 217–237.
<https://doi.org/10.1152/jn.1982.48.1.217>
- Aqil, M., Knapen, T., & Dumoulin, S. O. (2021). Divisive normalization unifies disparate response signatures throughout the human visual hierarchy. *Proceedings of the National Academy of Sciences*, 118(46), e2108713118. <https://doi.org/10.1073/pnas.2108713118>
- Avidan, G., Harel, M., Hendler, T., Ben-Bashat, D., Zohary, E., & Malach, R. (2002). Contrast Sensitivity in Human Visual Areas and Its Relationship to Object Recognition. *Journal of Neurophysiology*, 87(6), 3102–3116. <https://doi.org/10.1152/jn.2002.87.6.3102>
- Barrett, B. T., Bradley, A., & McGraw, P. V. (2004). Understanding the Neural Basis of Amblyopia. *The Neuroscientist*, 10(2), 106–117. <https://doi.org/10.1177/1073858403262153>

- Bazin, P.-L., Cuzzocreo, J. L., Yassa, M. A., Gandler, W., McAuliffe, M. J., Bassett, S. S., & Pham, D. L. (2007). Volumetric neuroimage analysis extensions for the MIPAV software package. *Journal of Neuroscience Methods*, 165(1), 111–121.
- Boynton, G. M., Demb, J. B., Glover, G. H., & Heeger, D. J. (1999). Neuronal basis of contrast discrimination. *Vision Research*, 39(2), 257–269.
- Brainard, D. H. (1997). The psychophysics toolbox. *Spatial Vision*, 10(4), 433–436.
- Broderick, W. F., Simoncelli, E. P., & Winawer, J. (2022). Mapping spatial frequency preferences across human primary visual cortex. *Journal of Vision*, 22(4), 3–3.
- Cameron, E. L., Tai, J. C., & Carrasco, M. (2002). Covert attention affects the psychometric function of contrast sensitivity. *Vision Research*, 42(8), 949–967.
[https://doi.org/10.1016/S0042-6989\(02\)00039-1](https://doi.org/10.1016/S0042-6989(02)00039-1)
- Campbell, F. W., & Robson, J. G. (1968). Application of Fourier analysis to the visibility of gratings. *The Journal of Physiology*, 197(3), 551–566.
- Carvalho, J., Invernizzi, A., Ahmadi, K., Hoffmann, M. B., Renken, R. J., & Cornelissen, F. W. (2020). Micro-probing enables fine-grained mapping of neuronal populations using fMRI. *Neuroimage*, 209, 116423.
- Chung, S. T. L., & Legge, G. E. (2016). Comparing the Shape of Contrast Sensitivity Functions for Normal and Low Vision. *Investigative Ophthalmology & Visual Science*, 57(1), 198.
<https://doi.org/10.1167/iovs.15-18084>
- Cimmer, C., Szendi, I., Csifcsák, G., Szekeres, G., Kovács, Z. A., Somogyi, I., Benedek, G., Janka, Z., & Kéri, S. (2006). Abnormal neurological signs, visual contrast sensitivity, and the deficit syndrome of schizophrenia. *Progress in Neuro-Psychopharmacology and Biological Psychiatry*, 30(7), 1225–1230.
- Cox, R. W. (1996). AFNI: Software for analysis and visualization of functional magnetic resonance neuroimages. *Computers and Biomedical Research*, 29(3), 162–173.
- Dale, A. M. (1999). Optimal experimental design for event-related fMRI. *Human Brain Mapping*, 8(2–3), 109–114.

[https://doi.org/10.1002/\(SICI\)1097-0193\(1999\)8:2/3<109::AID-HBM7>3.0.CO;2-W](https://doi.org/10.1002/(SICI)1097-0193(1999)8:2/3<109::AID-HBM7>3.0.CO;2-W)

- Dekker, T. M., Farahbakhsh, M., Atkinson, J., Braddick, O. J., & Jones, P. R. (2020). Development of the spatial contrast sensitivity function (CSF) during childhood: Analysis of previous findings and new psychophysical data. *Journal of Vision*, 20(13), 4–4.
- Dumoulin, S. O., Hoge, R. D., Baker Jr, C. L., Hess, R. F., Achtman, R. L., & Evans, A. C. (2003). Automatic volumetric segmentation of human visual retinotopic cortex. *Neuroimage*, 18(3), 576–587.
- Dumoulin, S. O., & Knapen, T. (2018). How Visual Cortical Organization Is Altered by Ophthalmologic and Neurologic Disorders. *Annual Review of Vision Science*, 4(1), 357–379. <https://doi.org/10.1146/annurev-vision-091517-033948>
- Dumoulin, S. O., & Wandell, B. A. (2008). Population receptive field estimates in human visual cortex. *Neuroimage*, 39(2), 647–660.
- Friston, K. J., Fletcher, P., Josephs, O., Holmes, A., Rugg, M. D., & Turner, R. (1998). Event-related fMRI: Characterizing differential responses. *Neuroimage*, 7(1), 30–40.
- Glover, G. H. (1999). Deconvolution of impulse response in event-related BOLD fMRI. *NeuroImage*, 9(4), 416–429. <https://doi.org/10.1006/nimg.1998.0419>
- Goulet, L. L., & Farivar, R. R. (2024). NeuroCSF: An fMRI method to measure contrast sensitivity function in human visual cortex. *bioRxiv*, 2024–01.
- Greene, C. A., Dumoulin, S. O., Harvey, B. M., & Ress, D. (2014). Measurement of population receptive fields in human early visual cortex using back-projection tomography. *Journal of Vision*, 14(1), 17–17.
- Henriksson, L., Nurminen, L., Hyvärinen, A., & Vanni, S. (2008). Spatial frequency tuning in human retinotopic visual areas. *Journal of Vision*, 8(10), 5–5.
- Hess, R. F., & Garner, L. F. (1977). The effect of corneal edema on visual function. *Investigative Ophthalmology & Visual Science*, 16(1), 5–13.
- Himmelberg, M. M., Winawer, J., & Carrasco, M. (2020). Stimulus-dependent contrast sensitivity asymmetries around the visual field. *Journal of Vision*, 20(9), 18–18.

- Himmelberg, M. M., Winawer, J., & Carrasco, M. (2022). Linking individual differences in human primary visual cortex to contrast sensitivity around the visual field. *Nature Communications*, 13(1), 3309.
- Hoffmann, M. B., & Dumoulin, S. O. (2015). Congenital visual pathway abnormalities: A window onto cortical stability and plasticity. *Trends in Neurosciences*, 38(1), 55–65.
- Hoffmann, M. B., Kaule, F. R., Levin, N., Masuda, Y., Kumar, A., Gottlob, I., Horiguchi, H., Dougherty, R. F., Stadler, J., & Wolynski, B. (2012). Plasticity and stability of the visual system in human achiasma. *Neuron*, 75(3), 393–401.
- Hou, F., Huang, C.-B., Lesmes, L., Feng, L.-X., Tao, L., Zhou, Y.-F., & Lu, Z.-L. (2010). qCSF in clinical application: Efficient characterization and classification of contrast sensitivity functions in amblyopia. *Investigative Ophthalmology & Visual Science*, 51(10), 5365–5377.
- Howell, E. R., Mitchell, D. E., & Keith, C. G. (1983). Contrast thresholds for sine gratings of children with amblyopia. *Investigative Ophthalmology & Visual Science*, 24(6), 782–787.
- Huang, C., Tao, L., Zhou, Y., & Lu, Z.-L. (2007). Treated amblyopes remain deficient in spatial vision: A contrast sensitivity and external noise study. *Vision Research*, 47(1), 22–34.
- Hyvärinen, L. (1983). CONTRAST SENSITIVITY IN VISUALLY IMPAIRED CHILDREN. *Acta Ophthalmologica*, 61(S157), 58–62.
<https://doi.org/10.1111/j.1755-3768.1983.tb03932.x>
- Ichhpujani, P., Thakur, S., & Spaeth, G. L. (2020). Contrast sensitivity and glaucoma. *Journal of Glaucoma*, 29(1), 71–75.
- Jigo, M., & Carrasco, M. (2020). Differential impact of exogenous and endogenous attention on the contrast sensitivity function across eccentricity. *Journal of Vision*, 20(6), 11.
<https://doi.org/10.1167/jov.20.6.11>
- Kay, K. N., Winawer, J., Mezer, A., & Wandell, B. A. (2013). Compressive spatial summation in human visual cortex. *Journal of Neurophysiology*, 110(2), 481–494.
<https://doi.org/10.1152/jn.00105.2013>
- Kleiner, R. C., Enger, C., Alexander, M. F., & Fine, S. L. (1988). Contrast sensitivity in age-related

macular degeneration. *Archives of Ophthalmology*, 106(1), 55–57.

Koskela, P. U., & Hyvarinen, L. (1986). Contrast sensitivity in amblyopia: III. Effect of occlusion. *Acta Ophthalmologica*, 64(4), 386–390.

<https://doi.org/10.1111/j.1755-3768.1986.tb06940.x>

Lee, S., Papanikolaou, A., Logothetis, N. K., Smirnakis, S. M., & Keliris, G. A. (2013). A new method for estimating population receptive field topography in visual cortex. *Neuroimage*, 81, 144–157.

Lerma-Usabiaga, G., Benson, N., Winawer, J., & Wandell, B. A. (2020). A validation framework for neuroimaging software: The case of population receptive fields. *PLoS Computational Biology*, 16(6), e1007924.

Lesmes, L. A., Lu, Z.-L., Baek, J., & Albright, T. D. (2010). Bayesian adaptive estimation of the contrast sensitivity function: The quick CSF method. *Journal of Vision*, 10(3), 17–17.

Leuba, G., & Garey, L. J. (1989). Comparison of neuronal and glial numerical density in primary and secondary visual cortex of man. *Experimental Brain Research*, 77(1).

<https://doi.org/10.1007/BF00250564>

Levitt, J. B., Kiper, D. C., & Movshon, J. A. (1994). Receptive fields and functional architecture of macaque V2. *Journal of Neurophysiology*, 71(6), 2517–2542.

<https://doi.org/10.1152/jn.1994.71.6.2517>

Marquardt, I., Schneider, M., Gulban, O. F., Ivanov, D., & Uludağ, K. (2018). Cortical depth profiles of luminance contrast responses in human V1 and V2 using 7 T fMRI. *Human Brain Mapping*, 39(7), 2812–2827. <https://doi.org/10.1002/hbm.24042>

Marques, J. P., Kober, T., Krueger, G., van der Zwaag, W., Van de Moortele, P.-F., & Gruetter, R. (2010). MP2RAGE, a self bias-field corrected sequence for improved segmentation and T1-mapping at high field. *Neuroimage*, 49(2), 1271–1281.

Milling, A., O'Connor, A., & Newsham, D. (2014). The importance of contrast sensitivity testing in children. *British and Irish Orthoptic Journal*, 11, 9–14.

Movshon, J. A., Thompson, I. D., & Tolhurst, D. J. (1978). Spatial and temporal contrast sensitivity

- of neurones in areas 17 and 18 of the cat's visual cortex. *The Journal of Physiology*, 283(1), 101–120. <https://doi.org/10.1113/jphysiol.1978.sp012490>
- Murphy, M. C., Conner, I. P., Teng, C. Y., Lawrence, J. D., Safiullah, Z., Wang, B., Bilonick, R. A., Kim, S.-G., Wollstein, G., & Schuman, J. S. (2016). Retinal structures and visual cortex activity are impaired prior to clinical vision loss in glaucoma. *Scientific Reports*, 6(1), 31464.
- Pedregosa, F., Eickenberg, M., Ciuciu, P., Thirion, B., & Gramfort, A. (2015). Data-driven HRF estimation for encoding and decoding models. *NeuroImage*, 104, 209–220. <https://doi.org/10.1016/j.neuroimage.2014.09.060>
- Pelli, D. G. (1997). The VideoToolbox software for visual psychophysics: Transforming numbers into movies. *Spatial Vision*, 10, 437–442.
- Pelli, D. G., & Bex, P. (2013). Measuring contrast sensitivity. *Vision Research*, 90, 10–14. <https://doi.org/10.1016/j.visres.2013.04.015>
- Pestilli, F., Viera, G., & Carrasco, M. (2007). How do attention and adaptation affect contrast sensitivity? *Journal of Vision*, 7(7), 9–9.
- Regan, D., Raymond, J., Ginsburg, A. P., & Murray, T. J. (1981). Contrast sensitivity, visual acuity and the discrimination of Snellen letters in multiple sclerosis. *Brain*, 104(2), 333–350.
- Ridder, A., Müller, M., Kotagal, V., Frey, K. A., Albin, R. L., & Bohnen, N. I. (2017). Impaired contrast sensitivity is associated with more severe cognitive impairment in Parkinson disease. *Parkinsonism & Related Disorders*, 34, 15–19.
- Rockel, A. J., Hiorns, R. W., & Powell, T. P. (1980). The basic uniformity in structure of the neocortex. *Brain: A Journal of Neurology*, 103(2), 221–244.
- Sclar, G., Maunsell, J. H., & Lennie, P. (1990). Coding of image contrast in central visual pathways of the macaque monkey. *Vision Research*, 30(1), 1–10.
- Singh, K. D., Smith, A. T., & Greenlee, M. W. (2000). Spatiotemporal frequency and direction sensitivities of human visual areas measured using fMRI. *NeuroImage*, 12(5), 550–564.
- Sirovich, L., & Uglesich, R. (2004). The organization of orientation and spatial frequency in primary visual cortex. *Proceedings of the National Academy of Sciences*, 101(48),

16941–16946. <https://doi.org/10.1073/pnas.0407450101>

- Sjöstrand, J. (1981). CONTRAST SENSITIVITY IN CHILDREN WITH STRABISMIC AND ANISOMETROPIC AMBLYOPIA. A STUDY OF THE EFFECT OF TREATMENT. *Acta Ophthalmologica*, 59(1), 25–34. <https://doi.org/10.1111/j.1755-3768.1981.tb06706.x>
- Sowden, P. T., Rose, D., & Davies, I. R. (2002). Perceptual learning of luminance contrast detection: Specific for spatial frequency and retinal location but not orientation. *Vision Research*, 42(10), 1249–1258.
- Stalin, A., & Dalton, K. (2020). Relationship of contrast sensitivity measured using quick contrast sensitivity function with other visual functions in a low vision population. *Investigative Ophthalmology & Visual Science*, 61(6), 21–21.
- Tootell, R. B., Reppas, J. B., Kwong, K. K., Malach, R., Born, R. T., Brady, T. J., Rosen, B. R., & Belliveau, J. W. (1995). Functional analysis of human MT and related visual cortical areas using magnetic resonance imaging. *Journal of Neuroscience*, 15(4), 3215–3230.
- Vasavada, V. A., Praveen, M. R., Vasavada, A. R., Shah, S. K., & Trivedi, R. H. (2014). Contrast sensitivity assessment in pediatric cataract surgery: Comparison of preoperative and early postoperative outcomes. *Journal of Cataract & Refractive Surgery*, 40(11), 1862–1867.
- Vinke, L. N., Bloem, I. M., & Ling, S. (2022). Saturating nonlinearities of contrast response in human visual cortex. *Journal of Neuroscience*, 42(7), 1292–1302.
- Wandell, B. A., Dumoulin, S. O., & Brewer, A. A. (2007). Visual field maps in human cortex. *Neuron*, 56(2), 366–383.
- Wang, G., Zhao, C., Ding, Q., & Wang, P. (2017). An assessment of the contrast sensitivity in patients with ametropic and anisometropic amblyopia in achieving the corrected visual acuity of 1.0. *Scientific Reports*, 7(1), 42043.
- Zimmern, R. L., Campbell, F. W., & Wilkinson, I. M. (1979). Subtle disturbances of vision after optic neuritis elicited by studying contrast sensitivity. *Journal of Neurology, Neurosurgery & Psychiatry*, 42(5), 407–412.

Zuiderbaan, W., Harvey, B. M., & Dumoulin, S. O. (2012). Modeling center-surround configurations in population receptive fields using fMRI. *Journal of Vision*, 12(3), 10.
<https://doi.org/10.1167/12.3.10>

Supplementary Materials

SF (c/deg)	Michelson contrast (%)											
0.5	0.25	0.39	0.61	0.95	1.48	2.30	3.58	5.58	8.70	13.56	32.94	80.00
1	0.25	0.39	0.61	0.95	1.48	2.30	3.58	5.58	8.70	13.56	32.94	80.00
3	0.25	0.39	0.61	0.95	1.48	2.30	3.58	5.58	8.70	13.56	32.94	80.00
6	0.25	0.61	0.95	1.48	2.30	3.58	5.58	8.70	13.56	21.13	32.94	80.00
12	0.25	0.61	1.48	2.30	3.58	5.58	8.70	13.56	21.13	32.94	51.33	80.00
18	0.25	0.61	1.48	2.30	3.58	5.58	8.70	13.56	21.13	32.94	51.33	80.00

Table S1. Stimulus contrast conditions. In each stimulus block gratings with the same spatial frequency (0.5, 1, 3, ,6, 12, or 18 c/deg) are shown but different Michelson contrast values. The contrast range presented was dependent on the spatial frequency shown in the stimulus block, ensuring an optimal sampling of the CSF (see Figure 1C).

HRF simulation

We used a default two-gamma HRF with five parameters: *time to peak gamma 1, full width at half maximum (FWHM) gamma 1, time to peak gamma 2, FWHM gamma 2, dip* (Friston et al., 1998; Glover, 1999). The standard values are set at *FWHM gamma 1 = 5.4 s, time to peak gamma 1 = 5.2 s, FWHM gamma 2 = 10.8 s, time to peak gamma 2 = 7.35 s, dip = 0.35 s*. We generated 50 HRFs by randomly selecting values for each of the five parameters. Each parameter was allowed to deviate from their standard value by a maximum of 30%, see Figure S1.

A combination of nCSF model parameters was chosen ($SF_p = 1$ c/deg, $CS_p = 150$ (a.u.), $width_R = 1.3$ (a.u.), $slope_{CRF} = 1.5$ (a.u.), see green curve in Figure 3) and a synthetic dataset was generated containing 100 voxel time series. We fitted the nCSF model to the synthetic dataset with each time a different HRF. The resulting nCSF estimates (normalized AUC , SF_p , CS_p , $slope_{CRF}$) as a function of *FWHM* and *time to peak* are shown in Figure S2. Normalized AUC , SF_p and $slope_{CRF}$ remain relatively constant when changing the *FWHM* and *time to peak* (see Figure S2 panels A, B, D, E, F ,H). However, $slope_{CRF}$ is systematically overestimated for both HRF parameters, indicating a more binary response. CS_p is decreasing with an increase in *FWHM* (see Figure S2C), but is relatively constant when changing time to peak (see Figure S2G). Overall, some parameters, in particular normalized AUC and SF_p , are more stable than others when changing *FWHM* and *time to peak* (in particular CS_p).

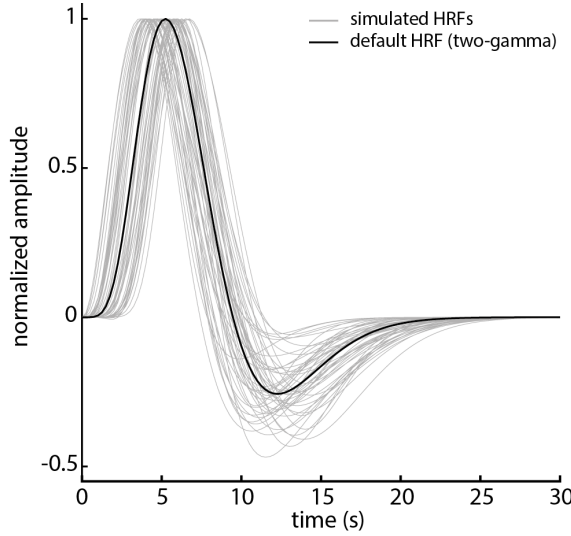


Figure S1. Simulated HRFs. The different HRFs used to estimate the nCSF model parameters. We generated 50 two-gamma HRFs by randomly selecting values for each of the five parameters, each parameter was allowed to deviate from their standard value by a maximum of 30%. The black line indicates the default two-gamma HRF (Glover, 1999), the gray lines represent the generated HRFs.

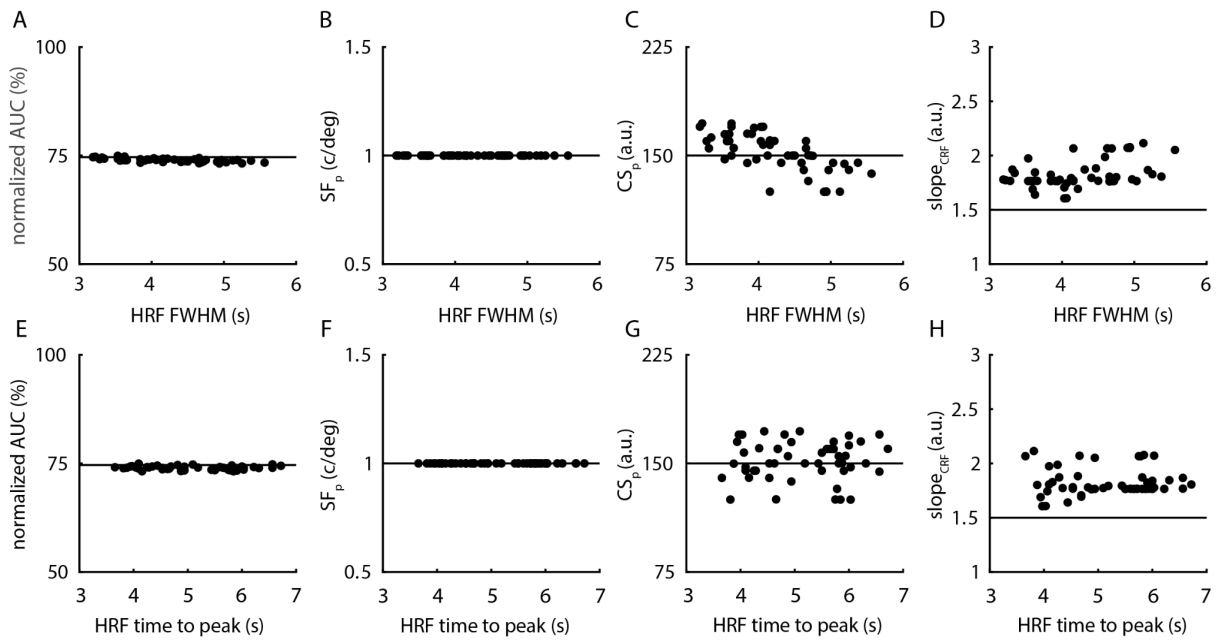


Figure S2. The relationship between the HRF model parameters and the nCSF model parameters. The effect of the HRF parameters (*FWHM* gamma 1 and *time to peak* gamma 1) on the nCSF model estimates: normalized *AUC*, SF_p , CS_p , $slope_{CRF}$). The line indicates the chosen value of the synthetic dataset. The dots represent the median values of 100 voxel time series. A) The effect of normalized *AUC* (c/deg) on *HRF FWHM* (s). B) The effect of SF_p (c/deg) on *HRF FWHM* (s). C) The effect of CS_p on *FWHM* (s). D) The effect of $slope_{CRF}$ on *HRF FWHM* (s). E) The effect of normalized *AUC* (c/deg) on *HRF time to peak* (s). F) The effect of SF_p (c/deg) on *HRF time to peak* (s). G) The effect of CS_p on *HRF time to peak* (s). H) The effect of $slope_{CRF}$ on *HRF time to peak* (s).

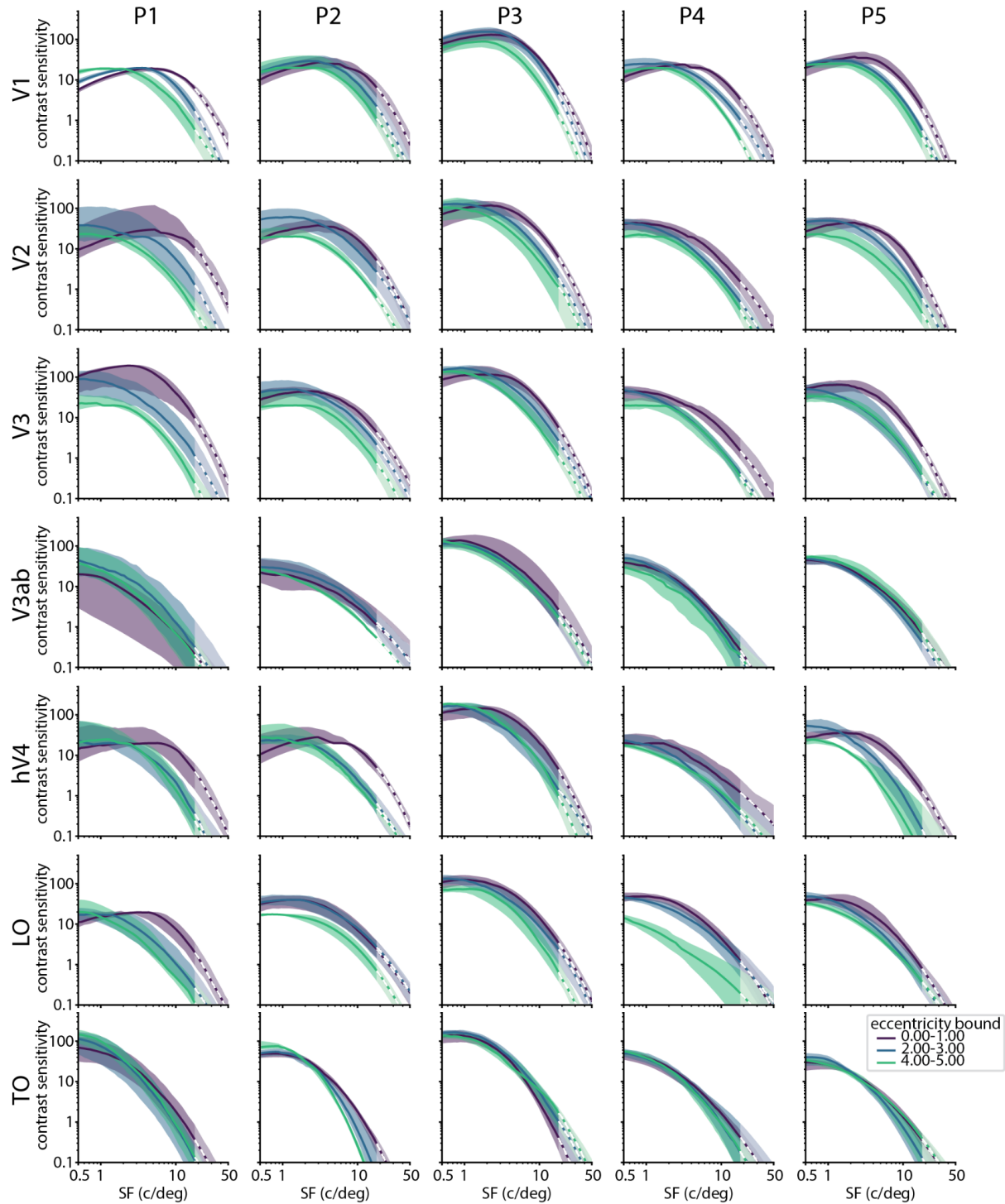


Figure S3. nCSF fits across eccentricities for all participants and ROIs. nCSF fits are split by eccentricity band (from pRF mapping: 0-1 degrees, 2-3 degrees, 4-5 degrees eccentricity; represented by purple, blue and green lines, respectively). Solid lines represent the median nCSF for all cortical locations within a given ROI and eccentricity band (where $r^2 > 30\%$). Shaded regions represent the 25th and 75th percentile of the nCSFs. We extrapolated the nCSF beyond the range of SFs present in the stimuli (>18 c/deg), where this has been done the lines become dotted and the shading becomes lighter.

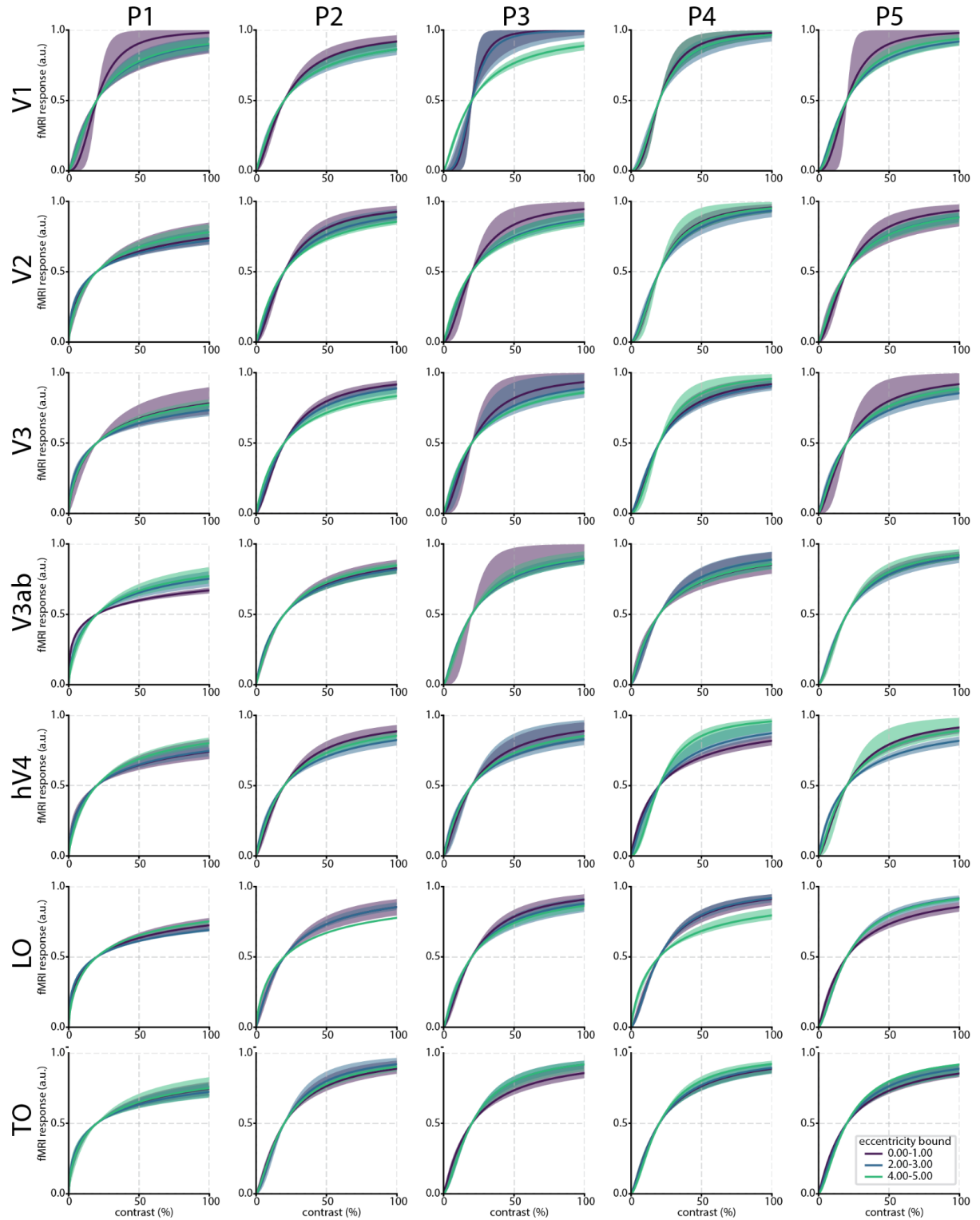


Figure S4. CRF fits across eccentricities for all participants and ROIs. CRF fits are split by eccentricity bands (0-1 degrees, 2-3 degrees, 4-5 degrees; represented by purple, blue and green lines, respectively). Solid lines represent the median CRF for all cortical locations within a given ROI and eccentricity band (where $r^2 > 30\%$). Shaded regions represent the 25th and 75th percentile of the CRFs.

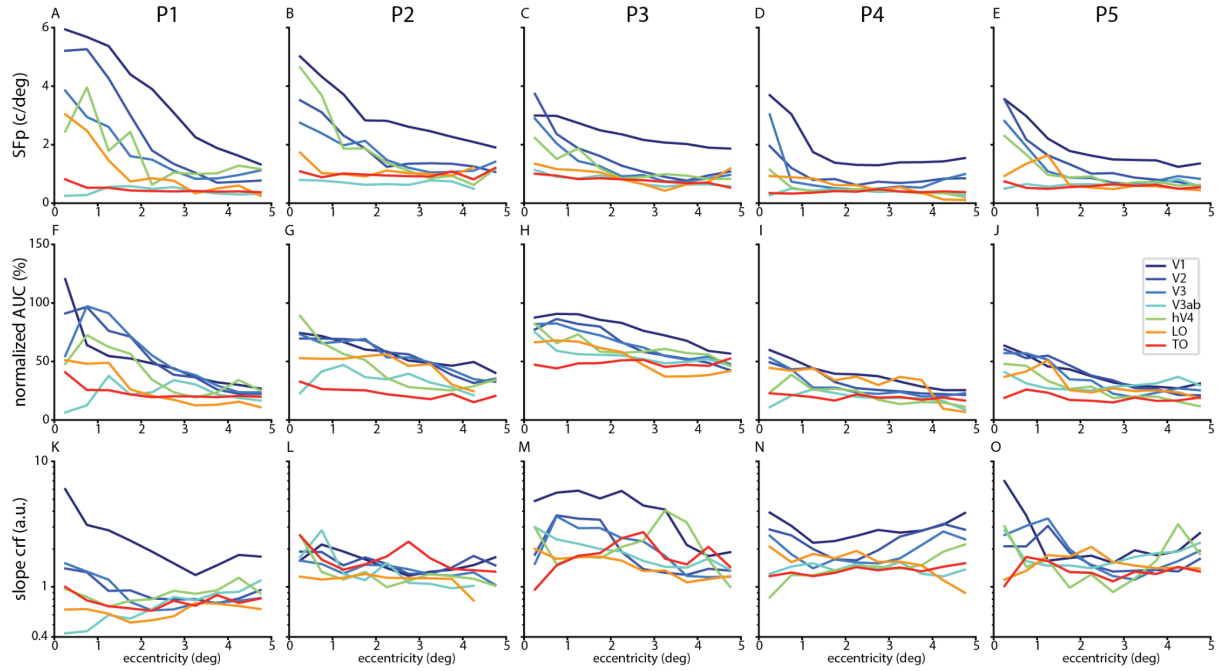


Figure S5. Variation nCSF properties across eccentricity and the cortical hierarchy. A-E) SF_p (c/deg) across eccentricity (deg) and ROIs for all participants (P1-P5). F-J) Normalized AUC (%) across eccentricity (deg) and ROIs for all participants (P1-P5). K-O) $slope_{CRF}$ (a.u.) across eccentricity (deg) and ROIs for all participants (P1-P5).

Slope of nCSF parameters with eccentricity in V1					
parameter	participant	eccentricity slope	t-statistic	p-value	degrees of freedom (adjusted)
AUC (%)	P1	-1.26	-30.02	<0.01	298.24
AUC (%)	P2	-11.86	-8.43	<0.01	298.24
AUC (%)	P3	-0.61	-6.85	<0.01	298.24
AUC (%)	P4	-0.68	-12.15	<0.01	285.86
AUC (%)	P5	-7.87	-11.7	<0.01	285.86
SF_p (c/deg)	P1	-0.16	-2.51	0.01	285.86
SF_p (c/deg)	P2	-0.28	-12.96	<0.01	380.98
SF_p (c/deg)	P3	-8.98	-17.54	<0.01	380.98
SF_p (c/deg)	P4	-1.12	-7.63	<0.01	380.98
SF_p (c/deg)	P5	-0.27	-8.52	<0.01	502.89
$slope_{CRF}$ (a.u.)	P1	-6.79	-21.16	<0.01	502.89
$slope_{CRF}$ (a.u.)	P2	0.13	1.56	0.12	502.89
$slope_{CRF}$ (a.u.)	P3	-0.46	-20.84	<0.01	465.75
$slope_{CRF}$ (a.u.)	P4	-8.24	-25.25	<0.01	465.75
$slope_{CRF}$ (a.u.)	P5	-0.53	-6.43	<0.01	465.75

Table S2. Results of linear regression of eccentricity on nCSF model parameters. Parameters explored are SF_p , AUC , and $slope_{CRF}$. Models are fit separately per participant, only including V1 cortical locations with a high variance explained (>30%). Degrees of freedom were obtained by taking the number of cortical locations in the ROI, and dividing by the volume-to-surface upsampling factor.

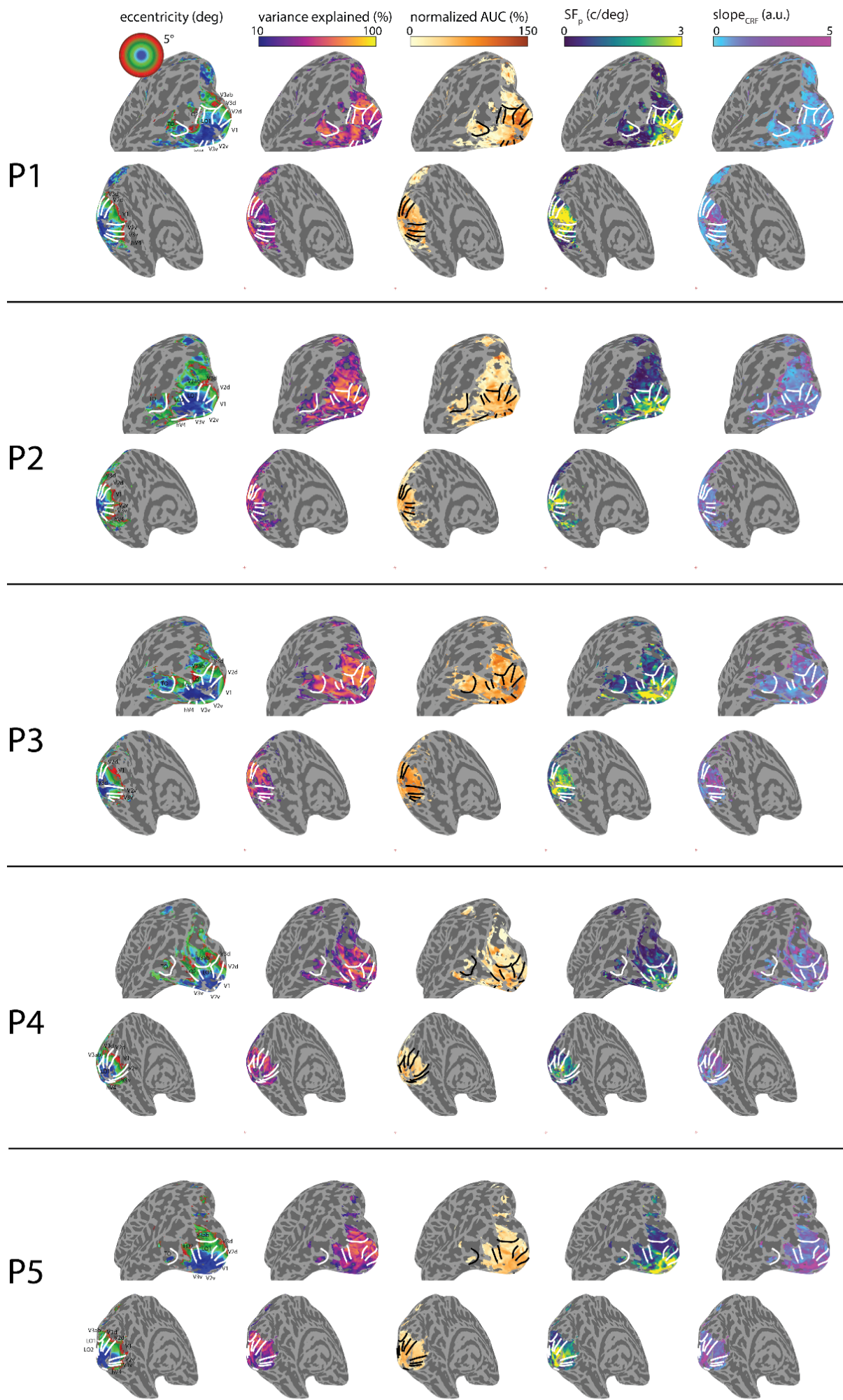


Figure S6. nCSF model parameters displayed on the cortical surface. Parameters are shown for all participants. We included cortical locations with variance explained >10% for visualization. Inflated cortical surfaces (left hemisphere) and ROIs with the lateral (top row) and medial (bottom row) views. Eccentricity (deg, from pRF mapping data) for comparison with nCSF parameters. Borders of ROIs (white lines) are displayed (V1, V2, V3, V3ab, hV4, LO, TO). Variance explained (r^2 %) of nCSF fits is high across ROIs and eccentricities. Panels D-F display nCSF model parameters: D) Normalized *AUC* (%), output variable). E) SF_p (c/deg). F) $slope_{CRF}$ (a.u.).